Draft version October 22, 2025
Typeset using LaTeX **twocolumn** style in AASTeX63

Steady Warps: Linear, Nonlinear, and Breaking

Jiaru Li [1] and Yoram Lithwick [1, 2]

[1] *Center for Interdisciplinary Exploration and Research in Astrophysics (CIERA), Northwestern University, 1800 Sherman Ave, Evanston, IL 60201, USA*

[2] *Department of Physics and Astronomy, Northwestern University, 2145 Sheridan Rd, Evanston, IL 60208, USA*

ABSTRACT

An increasing number of protoplanetary disks shows observational signatures of warps and misalignments, raising questions of how disks sustain coherent warps and how they may break into misaligned pieces. We study the steady-state structures and breaking conditions of warped disks. To focus on the hydrodynamics, while remaining agnostic about what forces the warp, we adopt a simple but physically motivated setup: rather than including an explicit perturber or external torque, we fix the disk inclination angles $\beta_{\rm in}$ and $\beta_{\rm out}$ at the inner and outer boundaries. The disk is hence constrained to accommodate a warp between the boundaries. By varying the boundary misalignment $|\beta_{\rm out} - \beta_{\rm in}|$, we can explore the linear regime, the nonlinear regime, and the onset of breaking, while having good control over the warp amplitude. Combining this model with analytical theories and three-dimensional hydrodynamic simulations, we carry out a clean and systematic investigation of the hydrodynamic behaviors of warped disks. We find that, with small warps, disks settle into warp steady states that are well described by the linear theory. Moderately warped disks enter the nonlinear regime, showing several distinct features such as torque saturation, vertical "bouncing" motion of gas, and enhanced mass accretion rates. Measurements of these effects in our simulations show good quantitative agreement with nonlinear theories. Strongly warped disks are unstable: these disks are susceptible to a runaway growth of warp amplitude that ultimately leads to disk breaking. This instability may be caused by the nonlinear saturation of the disk internal torque, which occurs roughly when the warp amplitude exceeds a critical value $|\psi|_{\rm crit} \simeq 2\sqrt{\alpha}$ for Keplerian disks.

1. INTRODUCTION

Accretion disks are not always flat; gas circulating the same central object at different radii may have different orbital inclinations, producing warped structures.

Recent observations have found an increasing amount of evidence that such warps commonly exist in protoplanetary disks. In near-infrared scattered light images, many disks exhibit non-axisymmetric dark regions (e.g., Marino et al. 2015; Stolker et al. 2017; Benisty et al. 2018; Casassus et al. 2018; Muro-Arena et al. 2020; Keppler et al. 2020; Kraus et al. 2020), which is often interpreted as shadows cast by warps (see Benisty et al. 2023). Complementary evidence comes from molecular line observations, through which several disks are found to have large-scale $m = 1$ velocity structures consistent with warped or non-planar gas flows (e.g., Panić et al. 2010; Pineda et al. 2014; Casassus et al. 2015; Winter et al. 2025). In addition, increasingly many systems have been revealed to host both warps and multiple misaligned disk components, pointing to a rich dynamical history involving both disk bending and breaking (e.g., Kraus et al. 2020; Muro-Arena et al. 2020; Bohn et al. 2022). Together, these observations raise two fundamental questions: how do disks bend and sustain coherent warps, and under what circumstances do they break into misaligned components?

Theories of warped disks have been developed over the past several decades (see, e.g., Nixon & King 2016, for an overview). In these studies, a warp is formally defined as the radial derivative of the disk inclination. Misaligned disk annuli can exert internal torques on each other (due to pressure, etc), which in turn drives the changes of the inclination profiles of the whole disk.

For nearly-Keplerian disks, how warp evolves depends on the viscous parameter α (Shakura & Sunyaev 1973) relative to the disk aspect ratio $h \equiv H/R$. Linear theories show that, for $\alpha \lesssim h$, warps can propagate as bending waves at approximately half of the sound speed, while being viscously damped at a rate $\sim \alpha\Omega$, where Ω is the angular velocity of the gas (Papaloizou & Lin 1995; Lubow & Ogilvie 2000). When $\alpha \gtrsim h$, viscous damping becomes strong enough to suppress wave propagation, so the warp instead evolves in a diffusive manner (Papaloizou & Pringle 1983). As a result, in the absence of external torques, free warps tend to flatten on the in-

termediate timescale between the orbital period $\sim \Omega^{-1}$ and the global viscous timescale $\sim (\alpha h^2 \Omega)^{-1}$. Warps in forced disks, on the other hand, may settle into steady states on the intermediate timescale if the relevant forcing acts more slowly (e.g., Lubow & Ogilvie 2000; Foucart & Lai 2014). Note that, if α is negligible, the evolution becomes sensitive to the difference between orbital and epicylic frequencies (i.e., the non-Keplerianity, see e.g., Ogilvie 1999, or Section 2). Hydrodynamic simulations have found good agreement with these linear theories (e.g., Lodato & Pringle 2007; Lodato & Price 2010; Kimmig & Dullemond 2024; Fairbairn 2025) .

The nonlinear regime, where warp amplitudes are large, is more complex and less well understood. Analytical theories predict several important nonlinear effects, such as modifications of the internal torques (Ogilvie 1999; Ogilvie & Latter 2013a; Dullemond et al. 2022), changes to the mass accretion flow (e.g., Pringle 1992; Ogilvie 1999), and the so-called "bouncing effect", in which gas elements would perform rapid vertical compression and expansion as they orbit around the star (Ogilvie & Latter 2013a; Fairbairn & Ogilvie 2021a,b; Held & Ogilvie 2024). These features have been identified in several numerical simulations (e.g., Lodato & Price 2010; Sorathia et al. 2013; Deng & Ogilvie 2022; Kaaz et al. 2023, 2025; Kimmig & Dullemond 2024). In low-α disks, wave coupling can also lead to parametric instability (Gammie et al. 2000; Ogilvie & Latter 2013b), which was not seen in the early numerical studies but emerged in recent high-resolution simulations (e.g., Paardekooper & Ogilvie 2019; Deng et al. 2021; Deng & Ogilvie 2022; Fairbairn & Stone 2025). Due to the complex nature of nonlinear hydrodynamics, recent studies tend to either pursue more powerful simulations (e.g., Deng & Ogilvie 2022; Kaaz et al. 2025) or develop alternative frameworks, such as affine models (Ogilvie 2018) and ring models (Fairbairn & Ogilvie 2021a).

Extreme nonlinear evolution can lead to disk breaking, where the disk splits into multiple disconnected planes (e.g., Larwood et al. 1996; Nixon et al. 2012, 2013; Zhu 2019; Liska et al. 2021). Several theories have been proposed to explain the mechanisms of breaking, including resonance with tidal forcing (Lubow & Ogilvie 2000; Martin et al. 2020), rapid nodal precession (Zhu 2019; Martin et al. 2020; Rabago et al. 2024), and linear instabilities related to the anti-diffusion of the disk density (Doğan et al. 2018; Raj et al. 2021). Yet a general condition and physical mechanisms that trigger disk breaking remain unclear.

In this paper, we focus on the long-lived warp steady state (WSS). Such states are more likely to be observable than their transient predecessors: given the lifetimes of protoplanetary disks, any warps present are likely to have relaxed into quasi-steady configurations. Our primary goals are to determine the WSS structures of disks, both in the linear and the nonlinear regimes, and to diagnose how a sufficiently large warp drives disk breaking.

We perform both theoretical analysis and numerical simulations. To focus on the hydrodynamics, while remaining agnostic about what forces the warp, we adopt a simple but physically motivated setup: rather than include an explicit perturber or external torque, we fix the disk inclination angles $\beta_{\rm in}$ and $\beta_{\rm out}$ at the inner and outer boundaries. The disk is hence constrained to accommodate a warp between the boundaries, and we can study the resulting steady-state structure. In the simulations, we also lower the surface density in the middle of the disk (but keep it non-empty), allowing us to localize the warp and reduce the possible influence of artificial boundary conditions. Our setup provides a clean laboratory for testing the hydrodynamic response of disks to generic perturbations. By varying the boundary misalignment $|\beta_{\rm out} - \beta_{\rm in}|$, we can explore the linear regime, nonlinear regime, and the onset of breaking, while having good control over the warp amplitude. As we will show, our simulations show excellent agreement with the theories.

The rest of this paper is organized as fellows. In Section 2, we discuss the theories of warped in disks in both linear and nonlinear regime. We perform hydrodynamic simulation for disks in linear, nonlinear and breaking regimes in Sections 3 to 5, respectively. Finally, we conclude in Section 6.

2. LINEAR THEORY

2.1. *Equations of Motion*

We focus on a disk with a steady warp. We imagine that the disk is forced to have unequal inclinations at its inner and outer boundaries, and study the resulting inclination profile in between. As discussed above, the timescale for the disk's inclination to reach its steady profile is much shorter than the disk's viscous time, and so we regard the surface density profile as a given time-independent function of radius.

The equations for the inclination have been derived many times (Pringle 1992; Ogilvie 1999; Fairbairn 2025, etc). We derive them again in Appendix A, because our assumption of a steady warp facilitates a conceptually simpler derivation, and allows us to proceed from first principles. Our derivation also makes clear that the resulting steady equations are equally valid whether $\alpha < h$ or $\alpha > h$, i.e., in the "wave-like" or "diffusive"

regimes. Here we summarize the derivation, highlighting the physical interpretation.

We adopt cylindrical coordinates (R, ϕ, z), a globally isothermal equation of state, and an α viscosity. We first solve for an unperturbed disk that is axisymmetric and aligned with the z axis. We then perturb the equations of motion to linear order, and assume that perturbed variables take on an $m = 1$ dependence in ϕ, and that their dependence on z is the leading term in a Hermite expansion. Higher-order Hermite terms, which have smaller vertical wavelengths, are suppressed by powers of the disk aspect ratio

$$h \equiv \frac{H}{R} \tag{1}$$

where H is the scale height. The perturbed radial and vertical velocities are then expressed as

$$\frac{v_R'}{\Omega R} = U_R \frac{z}{H} e^{-i\phi}, \tag{2}$$

$$\frac{v_z'}{\Omega R} = U_z e^{-i\phi} \tag{3}$$

where the coefficients U_R and U_z are functions only of R, $\Omega(R)$ is the unperturbed angular frequency (Equation A12), which for a globally isothermal disk is independent of z. Analogous expressions apply for v_ϕ' and the perturbed density (Equations A22 and A24). The resulting equations are reduced to two coupled equations for U_R and U_z (Equations A30 and A31). For reasons to be discussed shortly, we change dependent variables to

$$W \equiv -iU_z \tag{4}$$

$$U_r \equiv U_R + hU_z. \tag{5}$$

The resulting linear equations of motion are then

$$\frac{d}{dR}\left(\Sigma H R^3 \Omega^2 U_r\right) = 0, \tag{6}$$

$$(2\alpha + i\epsilon)\, U_r = H \frac{dW}{dR}, \tag{7}$$

where Σ is the imposed surface density, and ϵ quantifies the deviation of the epicyclic frequency from its Keplerian value. The expression for ϵ is given by Equation A13; it is typically small ($O(h^2)$), but can become big if $d\Sigma/dR$ is big. Rayleigh stability necessitates $\epsilon > -1$.

The variables W and U_r have clear physical interpretations. The former is the complex inclination. In other words, the disk's unit normal $\hat{\boldsymbol{l}}$ is, in Cartesian $[x, y, z]$ components

$$\hat{\boldsymbol{l}} \approx [\mathrm{Re}(W), \mathrm{Im}(W), 1] \tag{8}$$

to linear order in W.[1] Figure 1 (left panel) depicts the midplane of a warped disk with purely real W, meaning that it is not twisted. In this case, the maximum height at each radius lies at $y = 0$, as depicted by the dashed red line, which is repeated in the top right panel. The lower-right panels show the W profile, which in this case of real W is the usual (real-valued) inclination, and its warp ψ. For general complex W, the complex-valued warp is defined as

$$\psi \equiv \frac{dW}{d\ln R}. \tag{9}$$

In the figure, the warp is concentrated around $R \sim 1.5$. At much smaller or bigger R, the disk is unwarped, meaning that the disk tends to a flat plate, in which the inclination W is constant, and the maximum z is proportional to x.

The variable U_r quantifies sloshing motions that are in the "disk-horizontal" direction, i.e., perpendicular to $\hat{\boldsymbol{l}}$. As shown in Appendix A.3, the radial speed in the (spherical) $\hat{\boldsymbol{r}}$ direction is

$$\frac{v_r'}{\Omega R} = U_r \frac{z}{H} e^{-i\phi'}\ , \tag{10}$$

(after dropping $O(h^2)$ corrections) i.e., it has amplitude U_r. The dependence on z in Equation (10) indicates sloshing, in that the nearly-horizontal motion has an antisymmetric profile in z.[2] The sloshing is closely related to the torque (Lubow & Ogilvie 2000). We define the torque $\boldsymbol{G}$ as the angular momentum flux through a spherical shell. We show there that to linear order in W, and to leading order in h^2, one finds

$$\boldsymbol{G} \approx -\frac{1}{2}\Sigma H R^3 \Omega^2 \left[\mathrm{Re}(U_r), \mathrm{Im}(U_r), 0\right]. \tag{11}$$

We turn now to the interpretation of the two linear equations. Equation (6) states that the torque is independent of R. as may be seen by comparing with Equation (11). This must be true for a steady disk, as torque is the flux of angular momentum, and so if it varied with R it would necessitate time dependence. We note that

[1] In what follows, we shall define $\hat{\boldsymbol{l}}$ more precisely as the unit vector that is in the direction of the angular momentum of a spherical shell. See Equation (yyy) in the Appendix yyy for the full definition. We also show in that appendix that the resulting $\hat{\boldsymbol{l}}$ is given by Equation (8), to linear order in W, after dropping $O(h^2)$ corrections. [Need to make sure this is true].

[2] The reason v_r' rather than v_R' is relevant for sloshing may be appreciated by considering an unwarped disk (a flat plate) that is inclined relative to the $z = 0$ plane. In that case, $v_r' = 0$ as it is for an uninclined plate. But $v_R' \neq 0$ because inclining the disk introduces velocities in the R-direction that have the same z and ϕ-dependence as Equation (2).

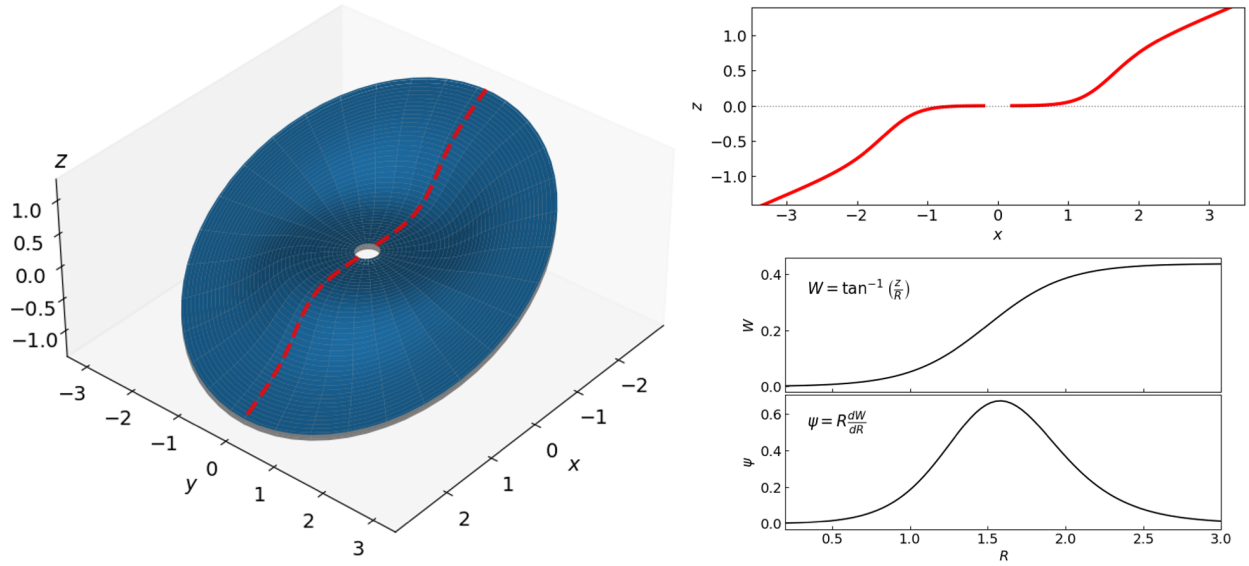

Figure 1. Midplane of a Warped Disk. This disk has no twist (W is purely real). **Left:** 3D diagram of the disk. The red dashed curve marks the maximum $|z|$ at each R, which lies along $y = 0$ for this untwisted disk. **Right Top:** Same as red-dashed curve in left panel. **Right Bottom:** Inclination and warp.

there is also a viscous contribution to the torque, but we drop it because it is subdominant (Appendix A.4).

Equation (7) states that the warp $\psi = dW/d\ln R$ drives sloshing. The dynamics may be appreciated by considering two neighboring circular rings in the midplane of a warped disk. Since their normals $\hat{\boldsymbol{l}}$ differ, from the perspective of one ring its neighbor moves up and down. That causes a disk-horizontal pressure gradient, which in turn forces the sloshing (see, e.g., discussion in Ogilvie & Latter 2013a, and their Figure 5). Equation (7) shows that for a given warp, the sloshing is $\propto 1/(2\alpha + i\epsilon)$, which is almost always very large in magnitude. The reason for this extreme reaction is that the vertical motions that accompany the warp are nearly resonant with free sloshing (epicyclic-type) motions in a nearly Keplerian disk (e.g., Papaloizou & Pringle 1983; Ogilvie 1999).

As discussed below, the linear equations break down when the warp is sufficiently big, $|\psi| \gtrsim \sqrt{\alpha}$ (ignoring ϵ). When that happens, the sloshing equation (Equation (7)) changes. We shall show that much—but not all—of the change is captured by the local nonlinear model of Ogilvie & Latter (2013a).

2.2. *Solution of the Linear Equations*

We re-express the linear equations in terms of the complex torque

$$G \equiv G_x + iG_y \approx -\frac{1}{2}\Sigma H R^3 \Omega^2 U_r, \tag{12}$$

in which case the equations are

$$\frac{dG}{dR} = 0, \tag{13}$$

$$(4\alpha + 2i\epsilon)\, G = -\Sigma H^2 R^3 \Omega^2 \frac{dW}{dR}. \tag{14}$$

The first equation has solution $G = \text{const}$. The second can then be integrated for the $W(R)$ profile. The boundary conditions are subtler. If the disk is not subject to external forcing, then $G = 0$ at the boundaries, and the steady solution is trivial, $W = \text{const}$, i.e., the disk is a flat plate, with constant inclination. On the other hand, an external perturber such as a planet or the outer disk can apply a torque, forcing G. The details depend on the perturber. But since we are interested in the disk's inclination profile rather than its interaction with a perturber, we adopt an equivalent, but conceptually slightly different, approach: we fix the inner and outer inclinations, and solve for $W(R)$ in between. Equation (14) gives

$$R\frac{dW}{dR} = \text{const}\frac{2\alpha + i\epsilon}{\Sigma R^2} \tag{15}$$

after adopting our globally isothermal assumption ($H\Omega$ =const). The right-hand side is a known function of R. Without loss of generality, we choose $W = 0$ at the inner boundary, and W to be purely real at the outer. Equation (14) is then integrated, with the constant in the equation adjusted to match the outer inclination. That adjustment is trivial for the linear problem.

Equation (15) shows that the warp is largest where ΣR^2 is smallest (ignoring ϵ for now). Intuitively, a

smaller Σ means that the disk is weaker, and the disk bends primarily where it is weakest. Figure 2 shows some solutions of the linear equations with three different assumed Σ profiles, which are shown in the top-left panel. We choose our domain to be

$$0.5 < R < 3 \tag{16}$$

and set

$$\alpha = 0.019, \tag{17}$$

$$h = 0.02 \times R^{1/2}, \tag{18}$$

where the latter is needed to obtain ϵ. The green Σ profile is a power law, $\Sigma \propto R^{-3/2}$. The resulting W and ψ are shown in the right panels. For this case, the warp $|\psi|$ is dominated at the inner boundary. More generally, for a power-law profile of Σ the warp is dominated at a boundary.

For the other two Σ profiles, we impose gaps of depth 0.2 and 0.05. As a result, the warp is concentrated in the gap, as may be seen in the right panels. For our later comparisons, it will prove convenient to keep the warp away from the domain boundaries, so that it is not affected by uncertain boundary conditions. We will do that by imposing a gap. But imposing a gap introduces a small complication: ϵ can get large at gap edges, as shown in the lower-left panel. Nonetheless, as long as $|\epsilon/\alpha| \ll 1$, as is true within most of the gap for the profiles shown, the effect of ϵ may be ignored there.

3. SIMULATIONS IN THE LINEAR REGIME

3.1. *Setup*

We perform 3D hydrodynamics simulations of warped disks using Athena++ (Stone et al. 2020) to study the behavior of disks at different warp amplitudes. The simulations solve the Navier-Stokes equations for a globally isothermal viscous disk in spherical polar coordinates (r, θ, ϕ). We perform 8 main simulations, which have parameters listed in Table 1. The radial domain spans from $r_{\rm in} = 0.5$ to $r_{\rm out} = 3$. The polar domain covers a range of θ with $\theta = \pi/2$ being the latitude of zero inclination. The azimuthal angle ϕ covers the full 2π range.

We take the thick black case in Figure 2 as our fiducial disk mode (i.e., $\Sigma \propto r^{-3/2}$ and gap depth 1/19). The disk is given an initial warp structure so that its orbital tilt, i.e., the direction of its orbital angular momentum vector, follows

$$\hat{\boldsymbol{l}} = [\sin(\beta)\cos(\gamma), \sin(\beta)\sin(\gamma), \cos(\beta)], \tag{19}$$

where $\beta = \arccos(\hat{\boldsymbol{l}} \cdot \hat{\boldsymbol{z}})$ is the orbital inclination β and $\gamma = \arctan2(\hat{\boldsymbol{l}} \cdot \hat{\boldsymbol{x}}, \hat{\boldsymbol{l}} \cdot \hat{\boldsymbol{y}})$ is the nodal angle.

We adopt a special radial boundary condition to hold the disk inclination to be zero at $r_{\rm in}$ and $\beta_{\rm out}$ at $r_{\rm out}$. These steady and non-coplanar boundaries force the disk to accommodate a finite warp to bridge its inner and outer parts, while also allowing the disk to evolve into a long-lived steady structure. In this way, we can directly study the general hydrodynamic behaviors of warped disks and avoid introducing scenario-dependent complexities. We use $\beta_{\rm out} = 0.033$ to test the linear theory. In later Sections we will also experiment with $\beta_{\rm out} \in \{0.1, 0.15, 0.2, 0.3, 0.4\}$ to cover the nonlinear regime.

Table 1 lists the simulations that we show in this paper. See Appendix C.1 for the details of the boundary implementation, Appendix C.2 for the details of the initial conditions, and Appendix C.3 for the time-integration scheme.

Table 1. Simulation parameters used in this study. The upper table lists parameter values that are common to all runs: the isothermal sound speed c_s, the viscosity parameter α at the center of the density gap ($r = 1.5$), and the radial coverage of the computational domain. The lower table summarizes the run-specific parameters: the disk inclination at the outer boundary $\beta_{\rm out}$ (radiant), the form of the α profile, the domain coverage in the θ direction, and the grid point numbers.

Parameter	sound speed c_s	viscous α	r-domain
Values	0.02	0.019	(0.5, 3.0)

Name	$\beta_{\rm out}$	$\alpha(r)$	θ-domain	(N_r, N_θ, N_ϕ)
C03	0.033	constant	(1.33, 1.81)	(256, 256, 260)
V03	0.033	variable	(1.33, 1.81)	(256, 256, 260)
C10	0.10	constant	(0.83, 2.31)	(256, 728, 260)
C15	0.15	constant	(0.83, 2.31)	(256, 728, 260)
C20	0.20	constant	(0.83, 2.31)	(256, 728, 260)
C30	0.30	constant	(0.83, 2.31)	(256, 728, 260)
C40	0.40	constant	(0.83, 2.31)	(256, 728, 260)

3.2. *Warp Structure*

We begin with examining disks with $\beta_{\rm out} = 0.033$ ($= 1.9°$), for which the warp is expected to be in the linear regime. We simulate two setups (C03 and V03 in Table 1): one with constant $\alpha = 0.019$ throughout the disk, and a non-fiducial one with a radially varying α. The radially varying α is to prevent the viscous filling of the initial density gap, so we set the variable $\alpha(r)$ by letting $\alpha\Sigma r^{3/2}$ be initially constant of r while keeping $\alpha = 0.0189$ at $r = 1.5$.

Figure 3 shows several diagnostics of the disk structure for both cases. The top panel shows the real-time

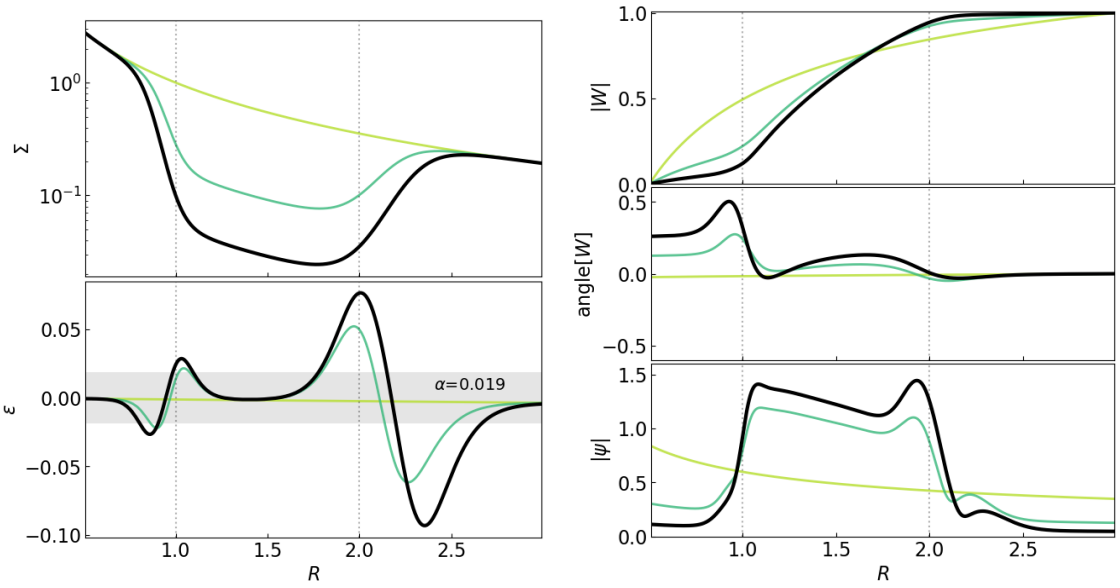

Figure 2. Examples of steady-state warp structures for disks with different background profiles. **Upper left:** Background surface density profiles of Σ. All disks are based on a power-law density $\Sigma \propto R^{-3/2}$, but applied with different density gaps (with gap edges marked with vertical dotted lines). **Lower left:** Background ϵ profiles calculated based on Σ; all disks adopts $\alpha = 0.19$, with the gray-shaded region shows where $|\epsilon| < \alpha$. **Top Right:** Steady-state $|W|$ profiles calculated from the linear steady-state Equations (6) and (7); we normalized the results to $|W| = 1$ at the $R = 3R_0$. **Middle Right:** Phase angle of the steady-state complex W. **Bottom Right:** Warp amplitude $|\psi|$ based on the $|W|$ profiles. We take the **thick black** case as our fiducial model.

disk surface density profile. For the variable-α case (left column), the density profile remains nearly unchanged in time, preserving the initial gap structure. In the constant-α case (right column), the surface density profile gradually evolves, slowly filling in the initial density gap. Eventually, the disk will reach a viscous steady state on the viscous timescale, for which the surface density is a power-law function of r.

The bottom three panels of Figure 3 show the inclination profile β, nodal angle γ, and the warp amplitude $|\psi|$. The disks are given initial inclination profiles $\beta(r) = \beta_{\rm out}(r - 0.5)/2.5$ and $\gamma = 0$. In the variable-α case, the β and $|\psi|$ profiles evolve into a long-term steady state, as shown by the orange curve at $t = 1256$ and the green curve at $t = 2550$. The phase angle γ is small and non-uniform in all snapshots, suggesting that the disk is weakly twisted. This steady warp structure approximately matches the linear-theory prediction shown by the gray curves, which is calculated from the (initially) background profiles.

For the constant-α case, the surface density is evolving over time. However, there still exists a warp steady state for each instantaneous density profile. The left column of Figure 3 shows that the simulated β and $|\psi|$ profiles (solid curves) are in excellent agreement with the real-time linear predictions (shown as light-colored curves), while the γ profile generally agrees, indicating that the disk can reach a warp steady state on a timescale much short than the viscous evolution timescale of the surface density. As the background slowly changes, the warp co-evolves adiabatically. This result predicts that astrophysical disks with long viscous timescales should be in their respective warp steady states.

Measurement details: Here we briefly describe how we measure the radial profiles of Σ, $\hat{\boldsymbol{l}}$, β, and ψ from our hydrodynamic simulations:

Surface density—To describe the spatial structure of the disk, we start with measuring the real-time disk surface density profile as

$$\Sigma(r) = \frac{r}{2\pi}\int_0^{2\pi}\int_0^{\pi}\rho\sin\theta d\theta d\phi, \tag{20}$$

where (r, θ, ϕ) are the spherical polar coordinates.

Tilt—The tilt profile can be calculated from a general fluid field as $\hat{\boldsymbol{l}} = \boldsymbol{L}/|\boldsymbol{L}|$, where

$$\boldsymbol{L}(r) = \frac{r^2}{2\pi}\int_0^{2\pi}\int_0^{\pi}\rho\boldsymbol{r}\times\boldsymbol{v}\sin\theta d\theta d\phi, \tag{21}$$

where $\boldsymbol{r}$ and $\boldsymbol{v}$ are the local position and velocity vectors.

Warp amplitude—We also calculate

$$|\psi| = \left|\frac{d\hat{\boldsymbol{l}}}{d\ln r}\right| \tag{22}$$

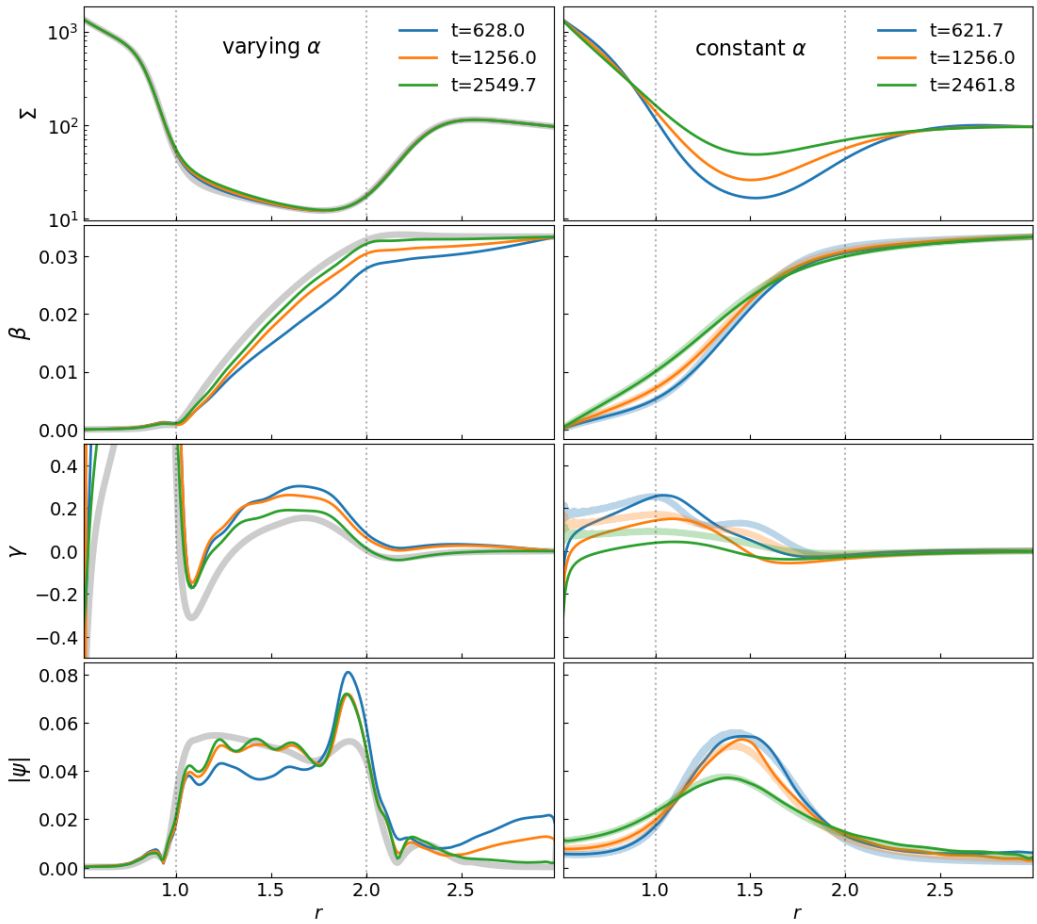

Figure 3. Evolution of a weakly warped disk with $\beta_{\rm out} = 0.033$ for variable (left, V03 in Table 1) and constant α profiles (right, C03 in Table 1). The solid-colored curves show the real-time surface density Σ (top row, measured using Equation 20), disk orbital inclination angle β, phase γ (two middle rows, Equation 19) and warp amplitude $|\psi|$ (bottom row, Equations 22) for both cases. In the left column, the faint-gray curves show the linear prediction $|W|$ for the variable-α disk at $t = 0$. The right column displays the linear theory prediction for the instantaneous steady-state solution $|W|$ as faint-colored curves.

as the warp amplitude. Note that this definition is the same as Equation 9 when β is small. It has also been used in several previous works (e.g., Ogilvie 1999).

3.3. *Sloshing and Torque*

To further test the linear theory, we examine the velocity and torque structure in the constant-α simulation (C03) at $t = 2461.7$.

Figure 4 shows the gas density ρ and the non-axisymmetric component of the radial velocity v_r' at $r = 1.5R_0$. The left panels show the raw fields at in the 2D (θ, ϕ) plane at $r = 1.5$, while the right panels display the same data transformed into a rotated frame where the disk midplane is placed at $\theta = \pi/2$. [3]

[3] Specifically, we plot the fields of $\rho(\boldsymbol{r}')$ and $v_r(\boldsymbol{r}')$ with $\boldsymbol{r}' = R_y(\beta)R_z(\gamma)\boldsymbol{r}$, where $\boldsymbol{r}$ is the position vector in the unrotated simulation frame and R_y and R_z are the rotational matrices around the $\hat{\boldsymbol{y}}$ and $\hat{\boldsymbol{z}}$ axis.

The density field in the simulation frame shows its midplane varying to different θ across the azimuth, which is a result of the disk inclination; in the rotated frame, the density field is almost axisymmetric (cf., Section bouncing).

The radial velocity field shows a sinusoidal variation in azimuth, which agrees with Equation (10). This pattern illustrates what has been referred to as the sloshing motion: as gas elements orbit around the star, they are driven by the disk warps to oscillate radially.

The sloshing motion v_r contributes to the radial transportation of angular momentum across the disk. The upper panel of Figure 5 shows the total radial flux of the angular momentum $\boldsymbol{G}$, measuredas

$$\boldsymbol{G}(r) = \frac{r^2}{2\pi}\int_0^{2\pi}\int_0^{\pi}(\boldsymbol{r}\times\boldsymbol{v})\,v_r\rho d\theta d\phi. \qquad (23)$$

The $\hat{\boldsymbol{x}}$ and $\hat{\boldsymbol{y}}$ components of the flux are mostly induced by the warp; they are constant at all r as predicted by

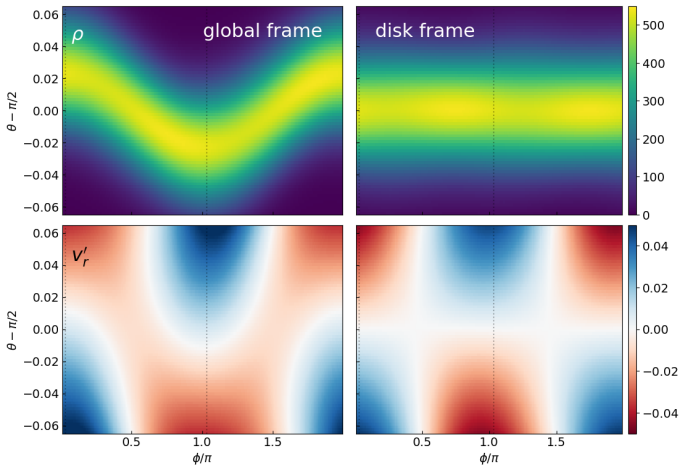

Figure 4. Density (top row) and velocity field (bottom row, shown as $v_r' = v_r - \langle v_r \rangle$ with $\langle v_r \rangle$ being the shell average of v_r) at $r = 1.5$ for the constant-α simulation at $t = 2461.7$. The left panels show the quantities in the simulation coordinates, while the right panels show the same data transformed into the local disk frame where the disk midplane is placed at $\theta = \pi/2$. The vertical dotted lines mark the ϕ angle where $\boldsymbol{U}_r$ is pointing.

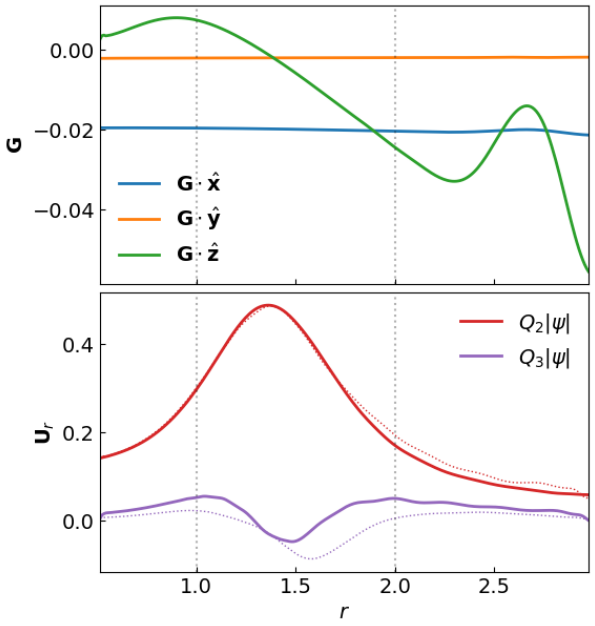

Figure 5. Internal torque $\boldsymbol{G}$ and the sloshing vector $\boldsymbol{U}_r$ in the constant-α simulation with $\beta_{\rm out} = 0.033$ at $t = 2461.7$ (i.e., C03 in Table 1). The upper panel shows the $\hat{\boldsymbol{x}}$-$\hat{\boldsymbol{y}}$-$\hat{\boldsymbol{z}}$ components of $\boldsymbol{G}$ (Equation 23). The lower panel shows the two components of $\boldsymbol{U}_r$, $Q_2|\psi|$ and $Q_3|\psi|$, with simulation measurement as solid and linear predictions (Equations 26 and 27) as dotted lines.

Equations (6) and (13), except at near the outer boundary. The $\hat{\boldsymbol{z}}$ component corresponds to background gas accretion, which is subdominant in magnitude.

The relation between $\boldsymbol{G}$ and ψ can be best shown by decomposing $\boldsymbol{G}$ into

$$\boldsymbol{G} = -\Sigma H^2 \Omega^2 r^2 \left[Q_1 \hat{\boldsymbol{l}} + \boldsymbol{U}_r \right] \tag{24}$$

with

$$\boldsymbol{U}_r = Q_2 \frac{\partial \hat{\boldsymbol{l}}}{\partial \ln r} + Q_3 \left(\hat{\boldsymbol{l}} \times \frac{\partial \hat{\boldsymbol{l}}}{\partial \ln r} \right), \tag{25}$$

where $\boldsymbol{U}_r$ is a vector characterizing the sloshing motion of the disk, while Q_1, Q_2, and Q_3 are dimensionless real numbers. These two equations are the more generalized form of Equation (11). Equations (7) predicts that

$$Q_2 = \frac{\alpha}{4\alpha^2 + \epsilon^2}, \tag{26}$$

$$Q_3 = \frac{1}{2} \frac{\epsilon}{4\alpha^2 + \epsilon^2}, \tag{27}$$

in the linear regime. The lower panel of Figure 5 compares the simulated $Q_2|\psi|$ and $Q_3|\psi|$ to their linear predictions, showing good agreement, especially inside the gap.

Fluid elements performing sloshing are on weakly elliptical orbits. The vector $\boldsymbol{U}_r$ is pointing at the phase angle where the radial velocity v_r is the maximum, i.e., the co-vertex (see Equation 10). Equation (25) implies that the disk warps along the co-vertex when Q_2 dominates Q_3 ($\alpha > |\epsilon|$), and along the apsis when Q_3 dominates ($\alpha < |\epsilon|$). We mark on Figure 4 the phase angle of $\boldsymbol{U}_r$, which coincides with where $|v_r'|$ is the largest and where the disk warps.

4. NONLINEAR REGIME

We also perform a suite of numerical simulations with $\beta_{\rm out}$ between 0.1 and 0.3 (5.7° to 17.2°, C10 to C30 in Table 1), for which the warp amplitudes are expected to be in the nonlinear regime. From now on we will focus on simulations with constant α, and we set up initial disk profiles using their linear steady-state solutions.

Figure 6 shows the resulted warp structure profiles from the simulations. As the disks reaches the WSS, their β and $|\psi|$ profiles both deviate from the linear-theory prediction.

4.1. *Saturation of Internal Torque*

The reason that causes the breakdown of the linear theory is the saturation of the disk's internal torque $\boldsymbol{G}$.

We define

$$|Q_4 \psi| = \frac{1}{\Sigma H^2 \Omega^2 r^2} |\boldsymbol{G}_\perp| \tag{28}$$

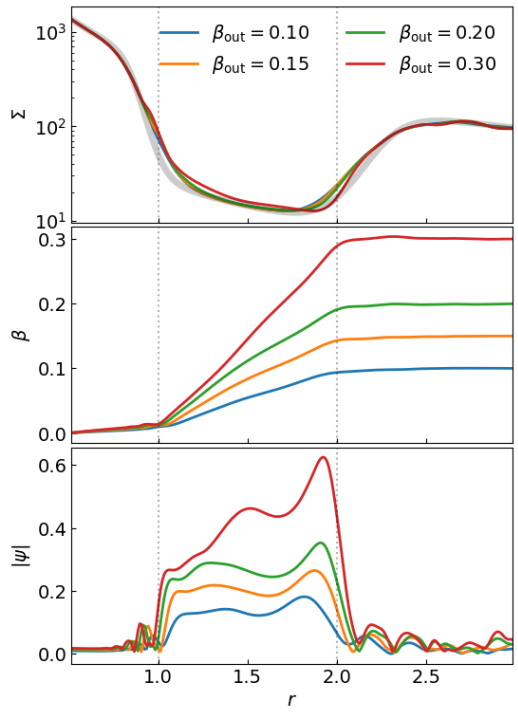

Figure 6. Surface density Σ, inclination profile β, and warp amplitude $|\psi|$ measured in moderately warped disks with different $\beta_{\rm out}$ (i.e., C10 to C30 in Table 1). The solid lines are the measurement at $t = 125.6$. The faint gray line in the top panel shows the initial density profiles.

as a dimensionless measure of the warp-induced torque amplitude. In the linear theory, $Q_4\psi = (Q_2 + iQ_3)\psi$ with Q_2 and Q_2 given by Equations (26) and (27). However, when the warp is strong, the disk may enter a *nonlinear* regime where Q_4 also depends on $|\psi|$, limiting the amplitude of $\boldsymbol{G}$ that the disk can attain.

This saturation process is seen in our nonlinear simulations. Figure 8 shows the measured $|Q_4\psi|$ profiles at $t = 125.6$ from the simulations, where we see that the amplitude of $|Q_4\psi|$ changes with on $\beta_{\rm out}$ nonlinearly. The difference between the $\beta_{\rm out} = 0.2$ (green) and the $\beta_{\rm out} = 0.3$ (red) cases is small, indicating a saturation of the $|Q_4\psi|$.

This nonlinear effect has been explored semi-analytically by Ogilvie & Latter (2013a) using a local shearing box model. Based on our real-time ψ profile, we solve their Equations (74) to (78) to get a prediction for the local fluid motions, and then use their Equation (92) to get a theoretical prediction for $|Q_4\psi|$. The results of the nonlinear predictions are displayed in Figure 8 as faint lines, which are in good agreement with the simulation results.

Figure 9 shows the relation between $|Q_4\psi|$ and $|\psi|$ in these simulations at a few locations inside the density gap. The open circles represent the measurement from the initial condition of the disk; all of them lay on the $|Q_4|$-vs-$|\psi|$ line predicted by the linear theory. The solid squares show the simulated values at $t = 125.6$, which all falls down to the nonlinear prediction curve.

4.2. *Bouncing Effects*

Figure 10 shows the density of the disks at $r = 1.5$. Stronger bouncing features emerge as $\beta_{\rm out}$ increases, with the density structure showing more extreme vertical compression and expansion along the azimuthal $\hat{\boldsymbol{\phi}}$ direction. We measure the bouncing amplitude through the local scale height $\tilde{H}$ of a disk, which is calculated as the standard deviation of the vertical density distribution, i.e.,

$$\tilde{H}(r,\phi) = \left[\frac{1}{\Sigma}\int_0^\pi \rho\,(\theta_{\rm mid} - \theta)^2\, r^3 d\theta\right]^{1/2}, \qquad (29)$$

where $\theta_{\rm mid}$ is the polar angle of the disk midplane. The measured maximum and minimum of H are shown in the panel for each case. In the most extreme case with $\beta_{\rm out} = 0.3$, the local scale height $\tilde{H}$ bounces between 0.011 and 0.097, while the unperturbed value is $H = 0.037$ at $r = 1.5$.

We use Equations (74) to (78) from Ogilvie & Latter (2013a) to calculate a theoretical predictions for the azimuthal scale height fluctuations using $\alpha = 0.019$, $\epsilon \simeq 0$ and the simulated $|\psi|$. The predicted $\tilde{H}$ are overplotted in Figure 10 as dotted lines, which match the simulation results with remarkable accuracy.

4.3. *Surface Density Evolution*

The simulation result also shows different Σ evolution for each different $\beta_{\rm out}$ (see the top panel of Figure 6). To quantify this difference, we measure the mass accretion rate,

$$\dot{M}(r) = \int_0^{2\pi}\int_0^\pi v_r \rho \sin\theta d\theta d\phi, \qquad (30)$$

inside the density gap (i.e., for r between 1 and 2). The results are shown in Figure 11.

We see that the accretion rate $\dot{M}$ is larger in disks with stronger warp, which is not a surprising result. As we have shown, warp can enhance angular momentum transport across the disk, so the disk density may need to redistribute accordingly by the conservation of total angular momentum. Based on the mass and angular momentum conservation, the predicted accretion rate $\dot{M}$ of a warped disk is given by (Ogilvie 1999)

$$\dot{M} = \frac{4\pi}{r\Omega}\frac{\partial}{\partial r}\left(Q_1 \Sigma H^2 r^2 \Omega^2\right) - 4\pi Q_2 \Sigma H^2 \Omega\,|\psi|^2, \qquad (31)$$

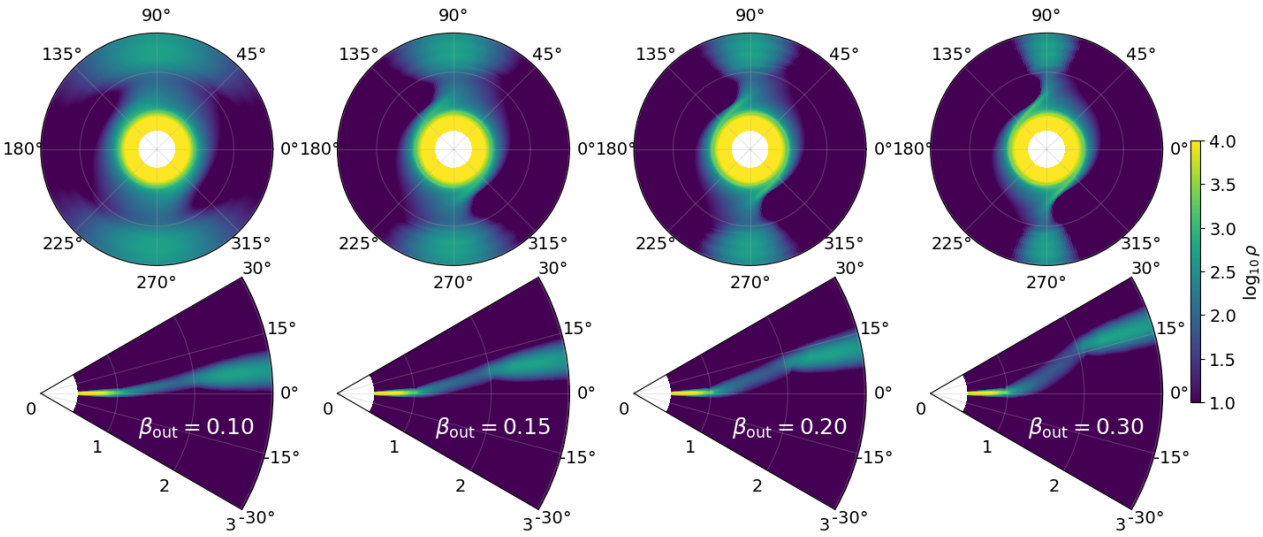

Figure 7. Snapshots of the volume density ρ at $t = 125.6$ for simulations in the nonlinear regime. Top and bottom row shows the cross section at $\theta = \pi/2$ and $\phi = 0$, respective. From left to right, the columns are from simulations with higher $\beta_{\rm out}$ values.

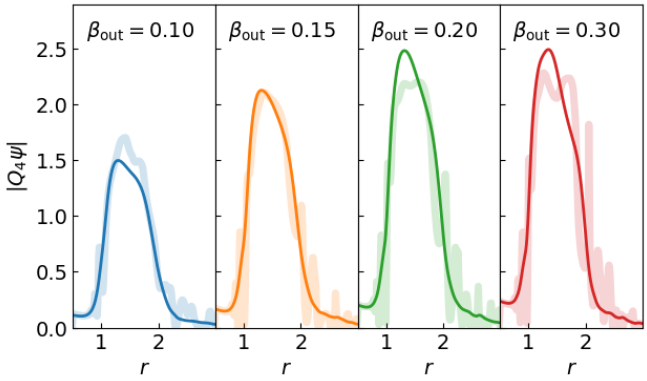

Figure 8. Radial profile of $|Q_4\psi|$ in simulations with constant α and different $\beta_{\rm out}$ (i.e., C10 to C30 in Table 1). The solid lines are the measurement at $t = 125.6$, while the faint lines are predictions based on Ogilvie & Latter (2013a)'s model, using mesured ψ and ϵ.

where

$$Q_1 = -\frac{1}{\Sigma H^2 \Omega^2 r^2} \boldsymbol{G} \cdot \hat{\boldsymbol{l}} \tag{32}$$

is a dimensionless coefficient that quantifies the $\hat{\boldsymbol{l}}$ component of $\boldsymbol{G}$.

The analytical values of Q_1 can be calculated from Equation (91) of Ogilvie & Latter (2013a). We use their model to calculate the analytical prediction of Q_1 and Q_2 using the real-time local values of $|\psi|$, and then we plug them into Equation (31) with the measured disk profiles to get a semi-analytical prediction for $\dot{M}$. The predicted values of $\dot{M}$ for a range of r are shown in Figure 11 as scattered boxes[4], which are in good agreement with the measured $\dot{M}$.

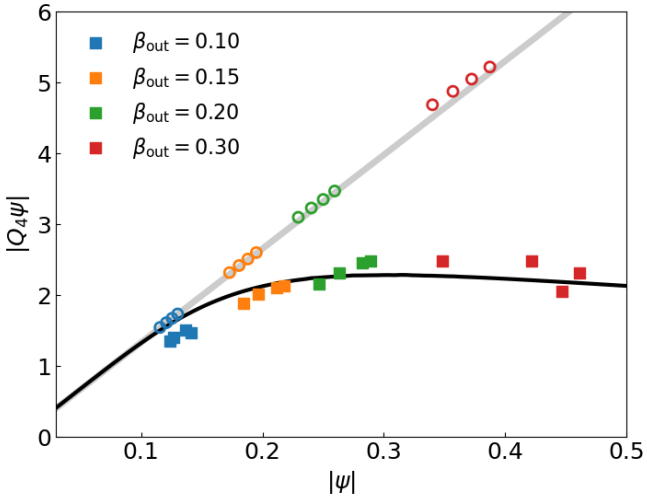

Figure 9. Relation between $|Q_4\psi|$ and $|\psi|$ in the nonlinear regime. The black line shows the prediction for $\alpha = 0.0189$ and $\epsilon = 0$ based on the shearing-box model in Ogilvie & Latter (2013a). The faint gray line represents the linear-theory relation. The scattered points show the values for $|Q_4\psi|$ and $|\psi|$ measured from the simulations. Each color represents one simulation with a different $\beta_{\rm out}$, while the dots with the same color correspond to the results measured at $r = 1.3$, 1.4, 1.5, and 1.6. The open circles and the solid squares shows the measurement at $t = 0$ and 125.8, respectively.

5. DISK BREAKING

[4] We assume $\epsilon = 0$ when calculate Q_1 and Q_2, so we only show the predicted $\dot{M}$ at r far away of the gas edges.

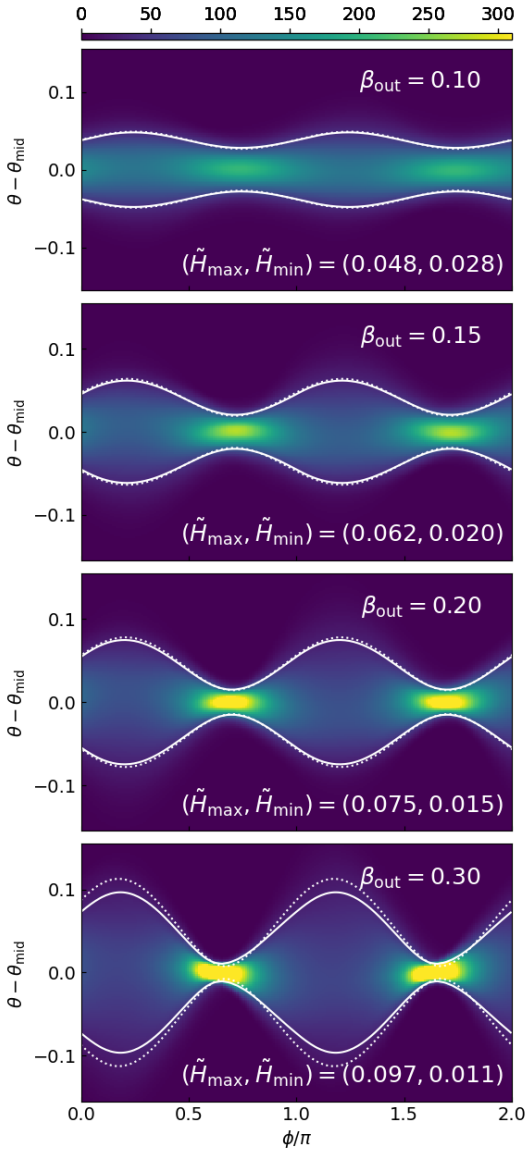

Figure 10. Simulated gas density distribution at $r = 1.5$ in four moderately warped disks at $t = 125.6$. The θ coordinates have been shift to place the disk midplane at the center of the vertical axis. The solid write lines trace the disk scale height measured using Equation (29), while the dotted lines are the predictions based on Ogilvie & Latter (2013a).

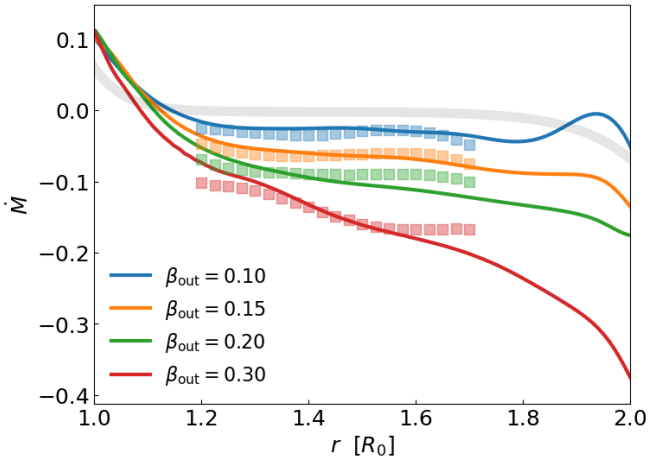

Figure 11. Mass flux $\dot{M}$ at the $t = 125.6$. The colored curves show measurements from the simulations using Equation (30), from $r = 1$ to 2. The scattered boxes represent the predictions based on the Equation (31), where we calculated Q_1 using the shearing-box model in Ogilvie & Latter (2013a) with the real-time local values of $|\psi|$, $\alpha = 0.019$, $\epsilon \simeq 0$. The faint gray curve corresponds to the theoretical accretion rate if we assume the disk is flat.

As we have seen in the previous section, large warp amplitude can leads to several nonlinear effects, including torque saturation, bouncing, and modified mass accretion flow. A natural question now is what happens if the warp increases even further? To explore this, we perform an additional simulations with a larger outer inclination angle $\beta_{\rm out} = 0.4$ (i.e., 23°, C40 in Table 1).

5.1. *Fiducial Simulation*

Figure 12 shows snapshots of the density field from the simulation; the top and bottom rows show the density distribution in the cross sections at $\theta = \pi/2$ and $\phi = 0$. The disk begins as a continuous warp ($t = 0$), similar to those in the earlier sections, except for the larger warp amplitude. As the system evolves ($t \sim 62.8$ to ~ 125.6), however, the inner and outer disk regions gradually detach, forming two disconnected planes separated by a narrow density gap at $r \simeq 1.5R_0$. After falling apart, the two disk portions quickly flatten themselves ($t \sim 188.4$), with the inner and our disks eventually aligned to $\beta_{\rm in} = 0$ and $\beta_{\rm out} = 0.4$, respectively.

Figure 13 illustrates the time evolution of the density, inclination, and warp amplitude profiles during the breaking process. The inclination profile β gradually steepen, eventually producing a sharp jump at the breaking point $r \simeq 1.5R_0$. The warp ψ initially spread nearly uniformly between $r = 1$ and $r = 2$; during the evolution, ψ becomes extremely localized, with the maximum $|\psi|$ increasing from ~ 0.5 at early times to as high as ~ 8 in the final snapshot. While the old density gap is filling up at $r \sim 1$ and ~ 2, a new sharp density gap gradually depletes at the breaking radius, where Σ decreases by a factor of ten, suggesting that mass flux is significantly enhanced by the strong warp.

We refer to this outcome, where the inner and outer disks detach in terms of β and the surface density depletes at the detaching point, as *disk breaking*. This breaking process is spontaneous: there is no explicit external forces tearing the disk, and the gravitational po-

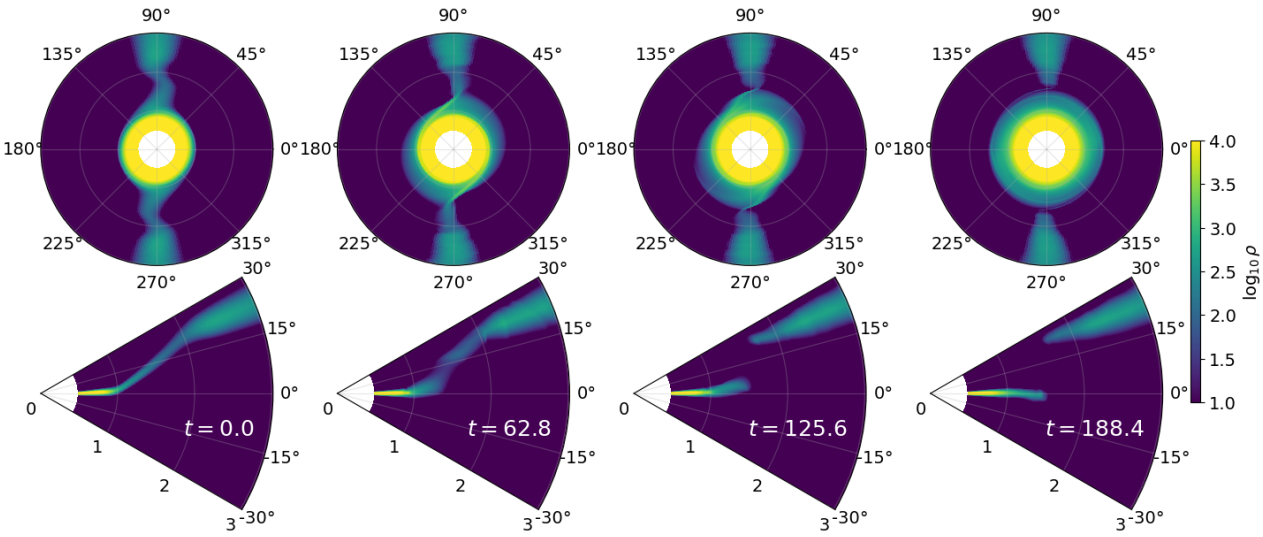

Figure 12. Snapshots of the density field ρ from the 'breaking' simulation with $\beta_{\rm out} = 0.40 = 23^\circ$ (i.e., C40 in Table 1). Top and bottom row shows the cross section at $\theta = \pi/2$ and $\phi = 0$, respective. The columns represents the time evolution from an initially connected disk ($t = 0.0$) to an eventually broken configuration ($t = 188.4$).

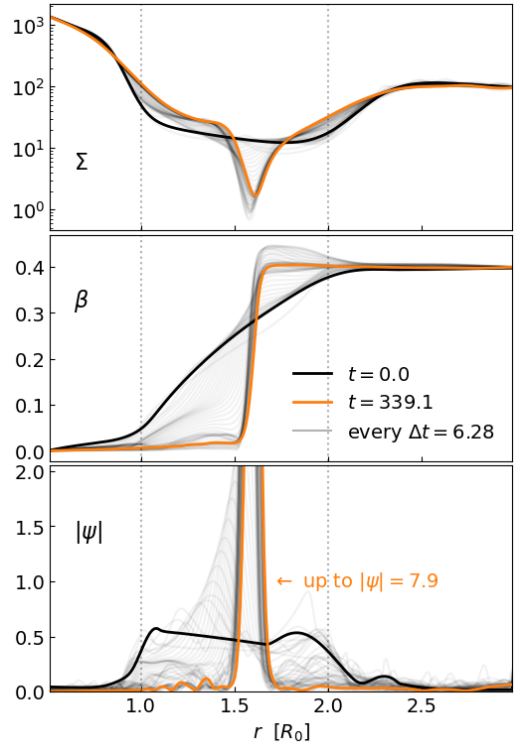

Figure 13. Surface density Σ, inclination profiles β, and warp amplitude $|\psi|$ measured in the simulaion with $\beta_{\rm out} = 0.4$ (i.e., C40 in Table 1). The black and orange lines are at $t = 0$ and $t = 339.1$, respectively. The faint gray curves shows the time evolution of the profiles at every $\Delta t = 6.28$.

tential is Keplerian. Hence, the breaking arises purely from internal hydrodynamics of the disk.

5.2. *1D Model for Disk Breaking*

5.2.1. *Breaking Mechanisms*

What leads the disk to break is the runaway growth of $|\psi|$. To understand that, we consider a set of toy-model time-evolution equations,

$$\Sigma R^2 \Omega \frac{\partial W}{\partial t} = -\frac{1}{R}\frac{\partial G}{\partial R}, \tag{33}$$

$$\frac{\partial G}{\partial t} + \alpha \Omega G = -\alpha \Sigma H^2 \Omega^3 R^2 Q_4 \psi, \tag{34}$$

where the first equation the conservation of angular momentum, the second is a nonlinear time-dependence version of Equation (7) (see Dullemond et al. 2022), and we have set $\epsilon = 0$ and assumed Q_4 is mostly real for simplicity.

Theories in previous Sections have been focused on the steady-state solution of Equations (33) and (34) with $G = -\Sigma H^2 \Omega^2 R^2 Q_4 \psi = \text{const}$. However, this solution is unstable against small perturbations when $\partial_\psi (Q_4 \psi) < 0$. We may performing a local stability analysis by assuming $G = G_0 + \delta G$ and $\psi = \psi_0 + \delta\psi$, where G_0 and ψ_0 are steady-state solutions and $\delta G, \delta\psi \propto e^{\gamma t + ikR}$ are small perturbations. Equations (33) and (34) suggest

$$\gamma \delta G + \alpha \Omega \delta G = -\Sigma H^2 \Omega^3 R \partial_\psi (Q_4 \psi)\, \delta\psi,$$
$$\Sigma R^2 \Omega \gamma \delta\psi = k^2 \delta G,$$

in the limit of large k. Solving for the growth rate γ shows that $\gamma > 0$ if $\partial_\psi (Q_4 \psi) < 0$. As similar result can be found in Doğan et al. (2018).

This instability conditions means, if a local increase in $|\psi|$ reduces the restoring torque, the warp would further amplify through a runaway growth. Consequently, the warp dominates at a particular radius $r_{\rm break}$, around

which the inner and outer disk parts are fully misaligned. The resulting large $|\psi|$ at $r_{\rm break}$ would also enhance the local $\dot{M}$ (see Equations 31), leading to a density depletion that disconnects the disk at the point of misalignment.

5.3. *Analysis*

The shearing-box model from Ogilvie & Latter (2013a) suggest that the critical warp amplitude for $\partial_\psi(Q_4\psi) < 0$ is about $|\psi|_{\rm crit} = 0.3$. Using the linear solution an estimate (see, e.g., the bottom right panel of Figure 2), our simulation with $\beta_{\rm out} = 0.4$ (C40) would have stead-state $|\psi| \approx 0.5$ and it indeed breaks. Our simulations with $\beta_{\rm out} \leq 0.2$ (C20) would have steadstate $|\psi| \approx 0.25$ and they do not break. These cases are consist with the implication of Ogilvie & Latter (2013a).

However, our simulation with $\beta_{\rm out} = 0.3$ is an exception to the simple breaking theory above. As indicated by the red squares in Figure 9, the simulated warp amplitudes are already above than the critical $|\psi|_{\rm crit}$ for $\partial_\psi(Q_4\psi) < 0$. Yet the disk does not break.

There are a few possible explanation to why this disk does not break. One example is that the instability is suppressed by shock. In a strongly warped (but not yet broken) disk, gas compresses and expands two times per orbit. At sufficiently large amplitude, these compression become supersonically and can produce shocks that damp the warp (Held & Ogilvie 2024; Kaaz et al. 2025), an effect that is not captured in our breaking theory. The disk with $\beta_{\rm out} = 0.3$ in our simulation may be a case when this damping is sufficient to offset the breaking process. Figure 9 shows that the steady state of this disk has $\partial_\psi|Q_4\psi|$ marginally less than zero, so it is possible that the instability is not enough to overcome the dissipation. This shock damping might also contribute to the small discrepancy in two $\tilde{H}$ curves shown in the bottom panel of Figure 10.

Figure 13 shows that, for the disk with $\beta_{\rm out} = 0.4$, the breaking radius is slowly moving outward. The rate of this outward drift appears faster in low-resolution runs. This trend suggests that the migration of the breaking radius at least partially controlled by resolution. A follow-up study may be needed to determine whether this drift is physical or purely numerical.

6. CONCLUSION

In this work, we have carried out a systematic investigation of warp steady states (WSS) in accretion disks, spanning the linear, nonlinear, and breaking regimes. Our study combines linear analytic theory, local nonlinear models, and global three-dimensional hydrodynamic simulations. Rather than including an explicit perturber or external torque, we fix the disk inclination angles $\beta_{\rm in}$ and $\beta_{\rm out}$ at the inner and outer boundaries. This setup provides a clean framework for diagnosing how the hydrodynamics of how disks bend, sustain coherent warps, and eventually break, while remaining agnostic about the origin of the warp.

For weakly warped disks, our simulations with $\beta_{\rm out} = 0.033$ confirm the linear theory. We see disks rapidly relaxing to their respective WSS; their simulated warping and inclination profiles, sloshing velocity fields and internal torque fluxes show excellent agreement with the theoretic predictions. Importantly, the predictions remain accurate for real-time steady-state warp profiles even as the background density slowly evolves, implying that protoplanetary disks should stay in quasi-steady warped states on timescales much shorter than their viscous evolution.

As we increase $\beta_{\rm out}$ to inject stronger warps, disks enter the nonlinear regime where several new features emerge. First, the internal torque no longer grows linearly with $|\psi|$, but instead it saturates. Second, the gas exhibits strong "bouncing" motions, undergoing cycles of vertical compression and expansion twice per orbital period; this effect leads to large azimuthal fluctuations in the local disk scale height. Third, large warp $|\psi|$ also enhance the mass accretion flows. All three effects are clearly measured in our simulations and are in good quantitative agreement with the nonlinear predictions (Ogilvie 1999; Ogilvie & Latter 2013a).

When the warp amplitude is increased further, nonlinear disks become unstable and may break. We show in our $\beta_{\rm out} = 0.4$ simulation that a strongly warped disk may undergo a runaway instability: the warp amplitude $|\psi|$ rapidly grows and localizes, and the disk eventually break into two misaligned pieces separated by a density gap. This breaking process occurs spontaneously from internal hydrodynamics, without requiring explicit external forcing. Our analysis suggest that this instability happens when the large warp causes the torque to fully saturate so that $\partial_\psi(Q_4\psi) < 0$; under this condition, local increases in $|\psi|$ reduce the restoring torque, rather than enhancing it. The critical warp amplitude for instability is given by $|\psi|_{\rm crit} \simeq 2\sqrt{\alpha}$ for Keplerian disks.

Overall, our work present a comprehensive picture of the hydrodynamics of warped disks, illustrating how disks may bend, sustain coherent warps, or break. One important topic for future studies is explore the long-term behavior of broken disks. Some previous simulations have shown examples where disks can heal from breaking and reconnect into whole pieces (e.g., Deng & Ogilvie 2022), but the exact mechanism is not fully understood. Future work may extend our results by incor-

porating additional physics, such as magnetic fields, turbulence, and gas self-gravity. Explicit perturbers may also be added to further connect our results to more specific astrophysical scenarios. One may also model the observational signatures of the nonlinear behaviors, such as bouncing and enhanced accretion, which may used for future detections of disk warping.

ACKNOWLEDGMENTS

We thank Diego Munoz, Jeremy Rath, Nicholas Kaaz, Rixin Li, and Alexander Dittmann for their stimulating discussion. Jiaru Li is supported by a CIERA Postdoctoral Fellowship. This work used computing resources provided by Northwestern University and the Center for Interdisciplinary Exploration and Research in Astrophysics (CIERA). This research was supported in part through the computational resources and staff contributions provided for the Quest high performance computing facility at Northwestern University which is jointly supported by the Office of the Provost, the Office for Research, and Northwestern University Information Technology.

APPENDIX

A. DERIVATION OF THE LINEAR THEORY

Here we derive the linearized equations of motion for a warp in a globally isothermal protoplanetary disk. The disk is governed by the momentum and continuity equations,

$$(\partial_t + \boldsymbol{v}_{\rm tot}\cdot\boldsymbol{\nabla})\,\boldsymbol{v}_{\rm tot} = -\boldsymbol{\nabla}\Phi - c_s^2\boldsymbol{\nabla}\lambda_{\rm tot}, \tag{A1}$$

$$(\partial_t + \boldsymbol{v}_{\rm tot}\cdot\boldsymbol{\nabla})\,\lambda_{\rm tot} = -\boldsymbol{\nabla}\cdot\boldsymbol{v}_{\rm tot}, \tag{A2}$$

where the subscript "tot" denotes the total value (background + perturbation), $\boldsymbol{v}_{\rm tot}$ is the velocity vector,

$$\lambda_{\rm tot} = \ln\rho_{\rm tot} \tag{A3}$$

is the logarithm of the density, c_s is the globally constant sound speed, and Φ is the gravitational potential of the central star. We temporarily ignore viscosity.

We shall decompose

$$\lambda_{\rm tot} = \lambda + \lambda' \tag{A4}$$

$$\boldsymbol{v}_{\rm tot} = \boldsymbol{v} + \boldsymbol{v}' \tag{A5}$$

where unsubscripted λ and $\boldsymbol{v}$ denote the background, and primed quantities denote the perturbation.

A.1. *Background*

The background is taken to be axisymmetric and aligned with the vertical axis. In cylindrical coordinates (R,ϕ,z), $\boldsymbol{v} = (v_R, v_\phi, v_z) = (0, R\Omega, 0)$. The angular frequency $\Omega(R,z)$ and $\lambda(R,z)$ are related by

$$R\Omega^2 = c_s^2\partial_R\lambda + \partial_R\Phi, \tag{A6}$$

$$0 = c_s^2\partial_z\lambda + \partial_z\Phi \tag{A7}$$

based on Equation (A1).

Taking ∂_z(A6) - ∂_R(A7) gives $\partial_z\Omega = 0$. Hence, Ω can be determined by evaluating Equation (A6) at the midplane, which yields

$$\Omega^2 = \Omega_{\rm K}^2 + \frac{c_s^2}{R}\partial_R\lambda_{\rm mid} \tag{A8}$$

where $\Omega_{\rm K} = \Omega_{\rm K}(R)$ is the Keplerian frequency and $\lambda_{\rm mid} = \lambda|_{z=0}$.

Taking $z\times$(A6) - $R\times$(A7) leads to

$$\partial_z \lambda = -\frac{z}{H^2} + \frac{z}{R}\partial_R \lambda, \tag{A9}$$

where

$$H = c_s/\Omega\ . \tag{A10}$$

Near the midplane of the disk, the first term on the right-hand side is dominant over the second as $H^2 \ll R^2$, so $\rho \propto \exp\left\{-z^2/(2H^2)\right\}$. Therefore, the background volume density of the disk has the form

$$\rho(R,z) = \frac{\Sigma}{\sqrt{2\pi}H}\exp\left\{-\frac{z^2}{2H^2}\right\}, \tag{A11}$$

where $\Sigma(R)$ is the radial profile of the disk surface density, which can be chosen freely.

In terms of Σ, Equation (A8) becomes

$$\Omega^2 = \Omega_{\rm K}^2 + \frac{c_s^2}{R}\partial_R \ln\left(\frac{\Sigma}{H}\right). \tag{A12}$$

We shall also need the epicyclic frequency,

$$\kappa^2 \equiv R^{-3}\partial_R(R^4\Omega^2) \tag{A13}$$

and its deviation from Ω via

$$\epsilon \equiv \frac{\kappa^2}{\Omega^2} - 1 \tag{A14}$$

$$= R\partial_R \ln(\Omega^2 R^3) \tag{A15}$$

$$\approx R\partial_R\left(\frac{H^2}{R^2}R\partial_R \ln\frac{\Sigma}{H}\right) \tag{A16}$$

where the final expression is to leading order in H^2/R^2 when $d_R(\ln\Sigma)$ is order unity.

A.2. *Perturbation Equations*

Linearizing Equations (A1) and (A2) yields

$$\partial_t v_R' = -\Omega\partial_\phi v_R' + 2\Omega v_\phi' - c_s^2\partial_R\lambda', \tag{A17}$$

$$\partial_t v_\phi' = -\Omega\partial_\phi v_\phi' - (2 + R\partial_R \ln\Omega)\,\Omega v_R' - \frac{c_s^2}{R}\partial_\phi\lambda', \tag{A18}$$

$$\partial_t v_z' = -\Omega\partial_\phi v_z' - c_s^2\partial_z\lambda', \tag{A19}$$

$$\partial_t \lambda' = -\Omega\partial_\phi\lambda' - \frac{1}{R}\partial_R\left(Rv_R'\right) - (\partial_R\lambda)\,v_R' - \frac{1}{R}\partial_\phi v_\phi' - (\partial_z\lambda)\,v_z' - \partial_z v_z', \tag{A20}$$

Following Tanaka et al. (2002) and Ogilvie (2008), we take the azimuthal dependency of linearized variables to be $\propto e^{-i\phi}$, as is appropriate for a warp, and we decompose the vertical dependency in Hermite polynomials. We further simplify by restricting the Hermite expansion to the leading-order contributions, which results in setting

$$\frac{v_R'}{\Omega R} = U_R\frac{z}{H}e^{-i\phi}, \tag{A21}$$

$$\frac{v_\phi'}{\Omega R} = U_\phi\frac{z}{H}e^{-i\phi}, \tag{A22}$$

$$\frac{v_z'}{\Omega R} = U_z e^{-i\phi}, \tag{A23}$$

$$\lambda' = \Lambda\frac{z}{H}e^{-i\phi}, \tag{A24}$$

where U_R, U_ϕ, U_z, and Λ are complex coefficients that depend on R and t. Plugging these into Equations (A17) to (A20) gives the evolution equations

$$\Omega^{-1}\partial_t U_R = iU_R + 2U_\phi + h^2 R(\partial_R \ln H)\Lambda - h^2 R\partial_R \Lambda, \tag{A25}$$

$$\Omega^{-1}\partial_t U_\phi = iU_\phi - (2 + R\partial_R \ln \Omega)\, U_R + ih^2\Lambda, \tag{A26}$$

$$\Omega^{-1}\partial_t U_z = iU_z - h\Lambda, \tag{A27}$$

$$\Omega^{-1}\partial_t \Lambda = i\Lambda - R\partial_R \ln\left(\Omega\Sigma H R^2\right) U_R - R\partial_R U_R + iU_\phi + \frac{1}{h}U_z - hR\partial_R \ln\left(\Sigma H^2\right) U_z, \tag{A28}$$

where

$$h = H/R \tag{A29}$$

is the aspect ratio. To derive Equation (A28), we use Equations (A9) and (A11) to calculate $\partial_z \lambda$ and $\partial_R \lambda$, respectively. In addition, although the factors of z cancel from the first three equations, some of the terms in Equation (A28) have coefficient z, and others have coefficient z^3. Since we are really extracting the projection of this equation onto the first Hermite polynomial, we replace those coefficients by their projections, which amounts to replacing $z \to H$ and $z^3 \to 3H^3$.

A.3. *Steady-State Equations*

Henceforth, we consider steady-state equations ($\partial_t \to 0$). Equation (A27) gives $\Lambda = iU_z/h$, which can be used to eliminate Λ in other three equations. We then eliminate U_ϕ by forming two different combinations of the three equations: $-i\times$(A25)$+2\times$(A26) and $-i\times$(A25)$+$(A26)$+$(A28). These combinations gives

$$0 = \frac{d}{dR}\left[\Sigma H\Omega^2 R^3 \left(U_R + hU_z\right)\right], \tag{A30}$$

$$0 = \frac{d\ln\left(\Omega^2 R^3\right)}{dR}\left(U_R + hU_z\right) + h\frac{d}{dR}U_z, \tag{A31}$$

which are two equations for two unknowns: $U_R + hU_z$ and U_z. The former is related to the radial speed in the (spherical) $\hat{\boldsymbol{r}}$ direction, $v_r' = (R/r)v_R' + (z/r)v_z'$, which implies

$$\frac{v_r'}{\Omega R} \approx \left(U_R + hU_z\right)\frac{z}{H}e^{-i\phi} \tag{A32}$$

after dropping the $O(z^2/r^2)$ correction. We therefore define

$$U_r \equiv U_R + hU_z \tag{A33}$$

which represents the amplitude of v_r'. Equations (A30–A31) then become

$$0 = \frac{d}{dR}\left(\Sigma H\Omega^2 R^3 U_r\right), \tag{A34}$$

$$0 = \epsilon U_r + hR\frac{d}{dR}U_z. \tag{A35}$$

We will show in A.4 that viscosity contributes an extra $-2i\alpha U_r$ term to the right-hand-side of Equation (A35).

Equations (6) and (7) then follow after defining

$$W \equiv -iU_z \tag{A36}$$

and including the viscous term.

A.4. *Viscous Terms*

Here, we derive the viscous term we added in the last step of the previous section. We take the viscous force per unit mass to be

$$\boldsymbol{f}_{\rm tot} = \frac{1}{R\Omega^2\rho_{\rm tot}}\boldsymbol{\nabla}\cdot\left(\nu\rho_{\rm tot}\boldsymbol{\tau}_{\rm tot}\right), \tag{A37}$$

where $\boldsymbol{\tau}$ is the stress tensor and ν is the kinematic viscosity,

$$\nu = \alpha c_s H, \tag{A38}$$

with α being the viscosity parameter as in the Shakura & Sunyaev (1973) model. This $\boldsymbol{f}_{\rm tot}$ is to be added to the right-hand side of Equation (A1).

We derive the perturbed $\boldsymbol{f}'$, which is to be inserted on the right-hand-side of the steady-state versions of Equations (A17)–(A19) by first working in the zero-inclination frame, where $v'_z = 0$. We shall then rotate to obtain the general form. Anticipating that the vertical viscous force is small, Equation (A19) implies $\lambda' = 0$. Then,

$$\boldsymbol{f}' = \frac{1}{R\Omega^2\rho}\boldsymbol{\nabla}\cdot(\nu\rho\boldsymbol{\tau}'). \tag{A39}$$

The most important terms in $\boldsymbol{\tau}'$ are

$$\tau'_{Rz} = \tau'_{zR} = \partial_z v'_R, \tag{A40}$$
$$\tau'_{\phi z} = \tau'_{z\phi} = \partial_z v'_\phi, \tag{A41}$$

as the main effect of viscosity is to act on the sloshing-induced vertical shear in the horizontal velocity components (see also Papaloizou & Lin 1995). Hence,

$$\boldsymbol{f}' \simeq \frac{1}{R\Omega^2\rho}\frac{\partial}{\partial z}\left[\nu\rho\left(\hat{\boldsymbol{R}}\partial_z v'_R + \hat{\boldsymbol{\phi}}\partial_z v'_\phi\right)\right] \tag{A42}$$
$$\simeq -\frac{\alpha z}{R\Omega}\left[\left(\partial_z v'_R\right)\hat{\boldsymbol{R}} + \left(\partial_z v'_\phi\right)\hat{\boldsymbol{\phi}}\right] \tag{A43}$$
$$\simeq -\frac{\alpha v'_R}{R\Omega}\left[\hat{\boldsymbol{R}} + \left(\frac{i}{2}\right)\hat{\boldsymbol{\phi}}\right], \tag{A44}$$

where we keep leading order terms by assuming $\partial_R, \partial_\phi \to \mathcal{O}(1)$ and $\partial_z \to \mathcal{O}(1/h)$ (see also Papaloizou & Lin 1995), and in the third equality we eliminate v'_ϕ by using the dominant contribution from Equation (A17).

In order to rotate $\boldsymbol{f}'$, we simply replace $v'_R \to v'_r$; other contributions to the rotation are higher order. The result is that Equations (A25)–(A26) are to be modified by adding to their respective right-hand-sides $-\alpha U_r$ and $\frac{1}{2}i\alpha U_r$. Finally, when we carry through the manipulations described in Section A.3, the viscous force adds $-2i\alpha U_r$ to the right-hand side of Equation (A35). It also adds a term to Equation (A34), but one that is smaller than the other in Equation (A34) term by $\mathcal{O}(\alpha)$, and so we drop it. Our viscous term is the same as those in Papaloizou & Lin (1995) and Lubow & Ogilvie (2000), except that their terms are proportional to U_R.

B. FROM COMPLEX-NUMBER NOTATION TO 3D TILT AND SLOSHING VECTORS

The linear theory in the main text adopts complex-number notations. This Appendix shows how to translate the complex linear quantities W and G into the real space vectors (tilt vector, etc).

B.1. *Tilt Vector* $\hat{\boldsymbol{l}}$.

The tilt vector is defined as $\hat{\boldsymbol{l}} = \boldsymbol{L}/|\boldsymbol{L}|$, where $\boldsymbol{L}$ is the total orbital angular momentum vector. The total orbital angular momentum at each disk radius is given by

$$\boldsymbol{L}(R) = \int_0^{2\pi}\int_{-\infty}^{+\infty} \boldsymbol{r}\times\boldsymbol{v}_{\rm tot}\rho_{\rm tot} R dz d\phi \tag{B45}$$
$$= \int_0^{2\pi}\int_{-\infty}^{+\infty} (\rho+\rho')\left(R\hat{\boldsymbol{R}} + z\hat{\boldsymbol{z}}\right)\times\left(v'_R\hat{\boldsymbol{R}} + \Omega R\hat{\boldsymbol{\phi}} + v'_\phi\hat{\boldsymbol{\phi}} + v'_z\hat{\boldsymbol{z}}\right) R dz d\phi \tag{B46}$$

where we have expanded the total fluid quantities into the background and the perturbation as in Equation (A4) in the second line. Adopting the perturbations given by Equations (A21) to (A24), we have

$$\boldsymbol{L} = \Sigma\Omega R^2\left[\mathrm{Re}(l_{xy}), \mathrm{Im}(l_{xy}), 1\right] \tag{B47}$$

where

$$l_{xy} = \frac{1}{2}\left(-iU_z + ihU_R - hU_\phi - h\Lambda\right) = -iU_z + \frac{3i}{4}hU_r + \mathcal{O}(h^2 U_z). \tag{B48}$$

The second equality holds when the disk is in a steady state so that $\Lambda = iU_z/h$ and $iU_R - hU_\phi = 3iU_r/2 + \mathcal{O}(hU_z)$ (based Equations A27, A25 and A33). By setting $W = -iU_z$ and the sloshing amplitude U_r with Equation (**??**), we get

$$l_{xy} = W + \mathcal{O}\left(h^2 W\right) + \mathcal{O}\left(\frac{h^2}{2\alpha + i\epsilon}\psi\right), \tag{B49}$$

where the last term is sub-dominate for small ψ and when $h \lesssim |2\alpha + i\epsilon|$ (i.e., when the resonance condition is not satisfied). Hence, we arrive at

$$\hat{\boldsymbol{l}} = \left[\mathrm{Re}(W), \mathrm{Im}(W), 1\right], \tag{B50}$$

which is introduced in Section **??** of the main text.

A similar calculation can be done in the spherical polar coordinates (r, θ, ϕ) for each spherical r, and we expect the spherical integral to give the same result when the aspect ratio $h \ll 1$ is small.

B.2. *Torque and Sloshing*

The angular momentum flux $\boldsymbol{G}$ is, at the leading order, given by

$$\boldsymbol{G} = \frac{1}{2\pi}\int_0^{2\pi}\int_{-\infty}^{+\infty}(\boldsymbol{r}\times\boldsymbol{v})\, v_r' \rho R dz d\phi, \tag{B51}$$

where the unprimed and primed quantities refer to the background and perturbations. The cross product can be expressed as

$$\begin{aligned}\boldsymbol{r}\times\boldsymbol{v} =& \hat{\boldsymbol{x}}(yv_z - zv_y) + \hat{\boldsymbol{y}}(zv_x - xv_z) + \hat{\boldsymbol{z}}(xv_y - yv_x) &\text{(B52)}\\ =& R\Omega\left[\hat{\boldsymbol{x}}(-z\cos\phi) + \hat{\boldsymbol{y}}(-z\sin\phi) + \hat{\boldsymbol{z}}(x\cos\phi + y\sin\phi)\right], &\text{(B53)}\end{aligned}$$

where we have dropped all v_z terms in the second line because they would be multiplied by v_r' and become second-order. For the velocity perturbation v_r' given by Equation (**??**), the flux is

$$\boldsymbol{G} = -\frac{1}{2}\Sigma H R^3 \Omega^2 \left[\mathrm{Re}(U_r), \mathrm{Im}(U_r), 0\right]. \tag{B54}$$

Note that, in hydrodynamical simulation, the $\hat{\boldsymbol{z}}$ component can be nonzero because v_r' may have axisymmetric ($m = 0$) components.

Inserting Equation (**??**) and $\psi = dW/d\ln R$ into (B54) gives

$$\frac{1}{\Sigma H^2 R^2 \Omega^2}\boldsymbol{G} = -Q_2\left[\mathrm{Re}\left(\frac{dW}{d\ln R}\right), \mathrm{Im}\left(\frac{dW}{d\ln R}\right), 0\right] - Q_3\left[-\mathrm{Im}\left(\frac{dW}{d\ln R}\right), \mathrm{Re}\left(\frac{dW}{d\ln R}\right), 0\right], \tag{B55}$$

where the first and the second vectors in the right-hand side are equal to $d\hat{\boldsymbol{l}}/d\ln R$ and $\hat{\boldsymbol{l}}\times d\hat{\boldsymbol{l}}/d\ln R$, respectively. Hence, we have

$$Q_2 = -\frac{1}{\Sigma H^2\Omega^2 R^2}\boldsymbol{G}\cdot\frac{\partial\hat{\boldsymbol{l}}}{\partial\ln R}, \tag{B56}$$

$$Q_3 = -\frac{1}{\Sigma H^2\Omega^2 R^2}\boldsymbol{G}\cdot\left(\hat{\boldsymbol{l}}\times\frac{\partial\hat{\boldsymbol{l}}}{\partial\ln R}\right), \tag{B57}$$

as shown by the Equations (**??**) and (**??**) in the main text, except that we use r instead of R when we analyze the hydrodynamic simulations.

B.3. *Apply Tilting*

Our hydrodynamic simulations initialize the disks with some tilting structure,

$$\hat{\boldsymbol{l}} = [\sin(\beta)\cos(\gamma), \sin(\beta)\sin(\gamma), \cos(\beta)]\,. \tag{B58}$$

For example, when we start the disk with linear steady-state warps, we let $\beta = |W|$ and $\gamma = \mathrm{Arg}(W)$.

To set up a disk with a desired $\hat{\boldsymbol{l}}(r)$ profile, we first construct a disk that is originally flat with its midplane placed at $\theta = \pi/2$, and then we tilt it. For a flat disk, its density ρ and velocity $\boldsymbol{v}$ are given by the background equilibrium. To tilt it, we rotate the fluid element at $\boldsymbol{r} = (r, \theta, \phi)$ to a new coordinate $\boldsymbol{r'} = (r, \theta', \phi')$ so that

$$\boldsymbol{r'} = \mathbf{R}_z(\gamma)\mathbf{R}_y(\beta)\boldsymbol{r}, \tag{B59}$$

where $\mathbf{R}_z(\gamma)$ and $\mathbf{R}_y(\beta)$ are the standard 3D rotational matrices around the $\hat{\boldsymbol{z}}$ and $\hat{\boldsymbol{y}}$ axes, respectively. When we calculate $\boldsymbol{r'}$, we convert $\boldsymbol{r}$ into cartesian coordinate so that apply $\mathbf{R}_z(\gamma)$ and $\mathbf{R}_y(\beta)$ can be applied; the result $\boldsymbol{r'}$ is also in cartesian coordinates, based on which we get spherical-polar coordinates (r, θ', ϕ'). As we rotate a fluid element from $\boldsymbol{r}$ to $\boldsymbol{r'}$, we change its velocity vector to

$$\boldsymbol{v'} = \mathbf{R}_z(\gamma)\mathbf{R}_y(\beta)\boldsymbol{v} \tag{B60}$$

and the preserve its density ρ.

When we analyze a simulation, we can reverse this tilting procedure using the real-time measured β and γ. This allows us to map from the simulation coordinates $\boldsymbol{r}_{\rm sim}$ to the disk midplane coordiantes $\boldsymbol{r}_{\rm disk}$ via

$$\boldsymbol{r}_{\rm disk} = \mathbf{R}_y(-\beta)\mathbf{R}_z(-\gamma)\boldsymbol{r}_{\rm sim}. \tag{B61}$$

This is how we obtain the disk-plane snapshots in the right panels of Figure 4 and in Figure 10.

C. DETAILS OF HYDRODYNAMIC SIMULATION SETUP

C.1. *Grid and Boundary Conditions*

Our simulations are preformed with Athena++ (Stone et al. 2020). We adopt spherical polar coordinates and uniformly spaced grid cells in r, θ and ϕ for our simulations. The azimuthal angle ϕ ranges from 0 to 2π while the radial r and polar θ coverages are given in Table 1. The ϕ domain is periodic; at each r and θ boundary of the domain, two ghost cells are attached outside the active mesh to implement boundary conditions.

The θ boundaries are placed sufficiently far from the disk midplane ($\geq 10H$ away from at $r = R_0$, $\geq 5.5H$ at $r = 1.5R_0$, and $\geq 2.5H$ at $r = 3.5R_0$) to ensure they do not influence the disk evolution. We impose reflective conditions, which are found to be the best for maintaining the vertical hydrostatic equilibrium of the disk and minimizing spurious inflows or outflows. Specifically, we copy the values of density ρ, radial velocity v_r, and azimuthal velocity v_ϕ from the last active cells into the ghosts, while the polar velocity v_θ is copied with its sign reversed. Similar boundary conditions have been used in a number of previous studies (e.g., Zhu 2019; Kimmig & Dullemond 2024).

The radial boundary condition needs to achieve two goals: (i) keeping the disk at fixed tilts, and (ii) allowing the sloshing motion to be consistent with the warp-steady-state condition. For (i), we hold the density values in the ghost cells at their initial values, so that the midplane of the disk is fixed. For (ii), we follow Equation (6) to set

$$\frac{v_r}{r\Omega} = U_r \propto \left(\Sigma H R^3 \Omega^2\right) = constant \tag{C62}$$

at the boundary.

In the following, we describe the details of our radial boundary implementation. We denote quantities associated with the first/last active cells with $'$ and those associated with the ghost cells with $''$. The density values in the ghost cells are held at their initial values, i.e.,

$$\rho'' = \rho''(t = 0). \tag{C63}$$

The velocity values in ghost cells are set in three steps: (1) calculate the cylindrical velocity components (v'_R, v'_ϕ, v'_z) with $\hat{\boldsymbol{z}}$ pointing at the direction of the disk plane (defined by $\beta = 0$ and $\beta = \beta_{\rm out}$ at the inner and outer boundaries,

respectively); (2) calculate these components for the ghost cells as

$$v''_R = v'_R \left(\frac{R''}{R'}\right)^{-1/2}, \tag{C64}$$

$$v''_\phi = v'_\phi \left(\frac{R''}{R'}\right)^{-1/2}, \tag{C65}$$

$$v''_z = 0, \tag{C66}$$

where the factor $-1/2$ is to keep U_r as a constant across the boundary based on Equation (C62); then (3) convert them to the spherical-polar components $(v''_r, v''_\theta, v''_\phi)$ and assign these values to the ghost cells. In short, this method is to set the ghost cell velocity to $\boldsymbol{v}'' = \left[\boldsymbol{v}' - \left(\boldsymbol{v}' \cdot \hat{\boldsymbol{l}}\right)\hat{\boldsymbol{l}}\right] \times (r''/r')^{-1/2}$, where $\hat{\boldsymbol{l}}$ is the target tilt at the boundary.

C.2. *Initial Conditions*

The initial disk is set in two steps: first setting up a disk in its flat background state, and then injecting a warp structure by tilting the disk.

We use an initial background surface density profile

$$\Sigma(r) = \Sigma_0 \left(\frac{r}{R_0}\right)^{-3/2} \frac{1}{f_{\rm gap}(r)}, \tag{C67}$$

where

$$f_{\rm gap}(r) = 1 + \frac{K-1}{2}\left[\tanh\left(\frac{r-R_a}{\Delta_a}\right) - \tanh\left(\frac{r-R_b}{\Delta_b}\right)\right] \tag{C68}$$

controls the shape of the gap. The parameters R_a and R_b are the locations of the inner and outer gap edges, Δ_a and Δ_b are the steepness of the edges, and the constant K determines the depth of the gap. We use parameter values $(R_a,\ R_b,\ \Delta_a,\ \Delta_b,\ K) = (R_0,\ 2R_0,\ 0.1R_0,\ 0.2R_0,\ 19)$ in all simulations. The background volume density is

$$\rho(r,\theta) = \frac{\Sigma(r)}{\sqrt{2\pi}H} \exp\left(-\frac{r^2\sin^2\theta}{2H^2}\right). \tag{C69}$$

To maintain this gap profile, we adopt a r-dependent α profile

$$\alpha(r) = \frac{\alpha_0}{K} f_{\rm gap}(r), \tag{C70}$$

which allows $\alpha = \alpha_0$ inside the gap and $\alpha = \alpha_0/K$ outside. The background azimuthal angular velocity is set to

$$\Omega^2(r) = \Omega_{\rm K}^2 \left(1 + \frac{c_s^2}{r^2\Omega_{\rm K}^2}\frac{\partial \ln \rho_{\rm mid}}{\partial \ln r}\right), \tag{C71}$$

to maintain radial force balance, while the initial radial and polar components are set to be zero.

The tilting step is then done by following the processes in Appendix B.3.

C.3. *Time Evolution*

Local-Lax-Friedrichs method (LLF) is adopted to solve the hydrodynamic equations in our simulations, where the spatial reconstruction of the primitive fluid quantities is done using the piecewise Linear Method (PLM). We perform time integrations using the second-order accurate Runge-Kutta/Heun's method (RK2). All of the numerical methods here are already implemented in public version of Athena++.

REFERENCES

Benisty, M., Juhász, A., Facchini, S., et al. 2018, A&A, 619, A171

Benisty, M., Dominik, C., Follette, K., et al. 2023, in Astronomical Society of the Pacific Conference Series, Vol. 534, Protostars and Planets VII, ed. S. Inutsuka, Y. Aikawa, T. Muto, K. Tomida, & M. Tamura, 605, doi: 10.48550/arXiv.2203.09991

Bohn, A. J., Benisty, M., Perraut, K., et al. 2022, A&A, 658, A183
Casassus, S., Marino, S., Pérez, S., et al. 2015, ApJ, 811, 92
Casassus, S., Avenhaus, H., Pérez, S., et al. 2018, MNRAS, 477, 5104
Deng, H., & Ogilvie, G. I. 2022, MNRAS, 512, 6078
Deng, H., Ogilvie, G. I., & Mayer, L. 2021, MNRAS, 500, 4248
Doğan, S., Nixon, C. J., King, A. R., & Pringle, J. E. 2018, MNRAS, 476, 1519
Dullemond, C. P., Kimmig, C. N., & Zanazzi, J. J. 2022, MNRAS, 511, 2925
Fairbairn, C. W. 2025, ApJ, 979, 156
Fairbairn, C. W., & Ogilvie, G. I. 2021a, MNRAS, 505, 4906
—. 2021b, MNRAS, 508, 2426
Fairbairn, C. W., & Stone, J. M. 2025, arXiv e-prints, arXiv:2506.08839
Foucart, F., & Lai, D. 2014, MNRAS, 445, 1731
Gammie, C. F., Goodman, J., & Ogilvie, G. I. 2000, MNRAS, 318, 1005
Held, L. E., & Ogilvie, G. I. 2024, MNRAS, 535, 3108
Kaaz, N., Liska, M. T. P., Jacquemin-Ide, J., et al. 2023, ApJ, 955, 72
Kaaz, N., Lithwick, Y., Liska, M., & Tchekhovskoy, A. 2025, ApJ, 979, 192
Keppler, M., Penzlin, A., Benisty, M., et al. 2020, A&A, 639, A62
Kimmig, C. N., & Dullemond, C. P. 2024, A&A, 689, A45
Kraus, S., Kreplin, A., Young, A. K., et al. 2020, Science, 369, 1233
Larwood, J. D., Nelson, R. P., Papaloizou, J. C. B., & Terquem, C. 1996, MNRAS, 282, 597
Liska, M., Hesp, C., Tchekhovskoy, A., et al. 2021, MNRAS, 507, 983
Lodato, G., & Price, D. J. 2010, MNRAS, 405, 1212
Lodato, G., & Pringle, J. E. 2007, MNRAS, 381, 1287
Lubow, S. H., & Ogilvie, G. I. 2000, ApJ, 538, 326
Marino, S., Perez, S., & Casassus, S. 2015, ApJL, 798, L44
Martin, R. G., Zhu, Z., & Armitage, P. J. 2020, ApJL, 898, L26
Muro-Arena, G. A., Benisty, M., Ginski, C., et al. 2020, A&A, 635, A121
Nixon, C., & King, A. 2016, in Lecture Notes in Physics, Berlin Springer Verlag, ed. F. Haardt, V. Gorini, U. Moschella, A. Treves, & M. Colpi, Vol. 905, 45, doi: 10.1007/978-3-319-19416-5_2
Nixon, C., King, A., & Price, D. 2013, MNRAS, 434, 1946
Nixon, C., King, A., Price, D., & Frank, J. 2012, ApJL, 757, L24
Ogilvie, G. I. 1999, MNRAS, 304, 557
—. 2008, MNRAS, 388, 1372
—. 2018, MNRAS, 477, 1744
Ogilvie, G. I., & Latter, H. N. 2013a, MNRAS, 433, 2403
—. 2013b, MNRAS, 433, 2420
Paardekooper, S.-J., & Ogilvie, G. I. 2019, MNRAS, 483, 3738
Panić, O., van Dishoeck, E. F., Hogerheijde, M. R., et al. 2010, A&A, 519, A110
Papaloizou, J. C. B., & Lin, D. N. C. 1995, ApJ, 438, 841
Papaloizou, J. C. B., & Pringle, J. E. 1983, MNRAS, 202, 1181
Pineda, J. E., Quanz, S. P., Meru, F., et al. 2014, ApJL, 788, L34
Pringle, J. E. 1992, MNRAS, 258, 811
Rabago, I., Zhu, Z., Lubow, S., & Martin, R. G. 2024, MNRAS, 533, 360
Raj, A., Nixon, C. J., & Doğan, S. 2021, ApJ, 909, 81
Shakura, N. I., & Sunyaev, R. A. 1973, A&A, 24, 337
Sorathia, K. A., Krolik, J. H., & Hawley, J. F. 2013, ApJ, 768, 133
Stolker, T., Sitko, M., Lazareff, B., et al. 2017, ApJ, 849, 143
Stone, J. M., Tomida, K., White, C. J., & Felker, K. G. 2020, ApJS, 249, 4
Tanaka, H., Takeuchi, T., & Ward, W. R. 2002, ApJ, 565, 1257
Winter, A. J., Benisty, M., Izquierdo, A. F., et al. 2025, arXiv e-prints, arXiv:2507.11669
Zhu, Z. 2019, MNRAS, 483, 4221